Room temperature ZnO ageing after Cold Sintering Process: Grain boundaries evolution characterization by in situ electrochemical impedance spectroscopy

Thomas Hérisson de Beauvoir, Claude Estournès

Room temperature ZnO ageing after Cold Sintering Process: grain boundaries evolution characterization by *in situ* Electrochemical Impedance Spectroscopy

Thomas Hérisson de Beauvoir, Claude Estournès

CIRIMAT, CNRS-INP-UPS, Université Toulouse 3 – Paul Sabatier, 118 route de Narbonne, 31062 Toulouse, France

Abstract:

The use of *in situ* characterization techniques is detrimental for the development of low temperature sintering techniques such as the Cold Sintering Process. This is particularly interesting for the investigation of interface regions, thus for grain boundaries. In the present work we focus on the evolution at room temperature, after the cold sintering of two ZnO ceramics sintered at 200 and 250 °C, and show the influence of the presence of remaining acetates on the final properties. Based on *in situ* impedance measurements at room temperature, the present results highlight the importance of paying attention to the behavior of cold sintered samples and their evolution after sintering, due to the potential presence of even small amounts (< 1 wt.%) of remaining liquid species that may strongly alter the final properties of the specimen, with almost 2 orders of magnitude resistivity increase.

1. Introduction

Lowering the sintering temperatures of ceramics has been pursued for years, not only for an energy consumption gain, but mainly in order to allow the fabrication of new types of devices, materials, composites, multilayers… Significant improvements were made with the introduction of low temperature sintering techniques such as Hydrothermal Hot Pressing [1–3], Hydrothermal Sintering [4,5], or low temperature Spar Plasma Sintering [6,7]. More recently, the Cold Sintering Process (CSP) was developed at PennState University by Randall's group [8–10], which represented a breakthrough in the field of low temperature sintering. Due to its technical simplicity and its high efficiency for the preparation of dense ceramics at extremely low temperature (< 400 °C and down to room temperature), it has attracted a major attention in literature. It has allowed the preparation on novel composite materials [11–13], new multilayer devices [14,15], and allowed in some cases to avoid grain growth and obtain extremely low grain sizes < 50 nm [16–18].

However, beyond its great efficiency, the mechanisms involved in this process remains complex and still not perfectly understood [19–21]. Although it appears clear that the sintering proceeds through dissolution-precipitation phenomenon [22], there is still some open questions about the nature of interfacial reactions (solid-liquid interfaces) and grain boundary formation process. These interfaces, that lie at the core of the cold sintering process efficiency, may be highly changed by the sintering conditions, therefore leading to altered properties, despite an important densification level [8]. This brought the attention towards the importance of paying attention not only to the densification and grain sizes to determine the properties of ceramics, but also their grain boundary (GB) nature, composition and quality.

This reaction complexity is well exemplified in by the work of Funahashi *et al.* [23] where the authors showed the full densification of ZnO in the presence of acetic acid, while no densification could be obtained in pure water by using the CSP. In another work by Gonzalez-Julian *et al.* [24] demonstrated by FAST/SPS the possibility to densify ZnO at only 250 °C, both in acetic acid or pure water, by using lower amount of liquid phase and higher temperature ramps, avoiding the grain growth in the case of pure H_2O as a liquid phase.

These modifications of sintering conditions may have an influence on the properties of the sintered ceramics. For instance, in the application of CSP to ZnO with various liquid phases, it has been shown that samples sintered with acetic and formic acid, although they have similar densities, their mechanical fracture toughness can be doubled (from acetic to formic acid) [25]. This shows the importance of considering the interfaces formed during the CSP. In addition, Jing *et al.* [26] showed the possibility to increase by 4 orders of magnitude the conductivity of ZnO ceramics as-cold sintered and post annealed samples at 500 °C. All of these observations highlight the importance of paying attention to GB interfaces during CSP.

However, not much attention has been paid to the evolution of interfaces with time, after cold sintering. In conventional sintering techniques, the temperatures involved to densify materials are sufficiently high to remove any liquid and/or organic phase from the samples. This induces more intrinsic interface/grain boundary stability over time at room temperature. Oppositely, the Cold Sintering Process involves the presence of liquid phase during sintering, that may or may not be completely removed during sintering thermal cycle. This may lead to room temperature evolution of grain boundaries, similar to what occurs in the case of low temperature degradation of zirconia ceramics for biomedical implants [27]. Therefore, there is a need for focused studies in the field of ageing effects on low temperature sintered materials.

To analyze these GB formation and evolution, *in situ* impedance spectroscopy analysis setup was introduced in our group [28] to measure the evolution of GB and solid-liquid interfaces contributions to impedance during the sintering dwell time. This was applied to CSP of ZnO in the presence of acetic acid, and allowed to highlight the conditions for acetate species elimination, changing the final properties of the samples after cold sintering in various temperatures ranging from 150 to 250 °C. However, this work did not explore the evolution of these properties after cooling down to room temperature and its evolution with time. In the present work, we continue this work, and investigate the impedance evolution of cold sintered ZnO after sintering. Then, structural, microstructural and optical properties of the prepared materials were characterized in order to explain the observations made by impedance.

2. Experimental

The sample preparation and characterization were done accordingly to the work described in [28]. ZnO was obtained from Alfa Aesar (99%) with particle size of 40-100 nm and acetic acid from Sigma Aldrich (>99%). Acetic acid was mixed with distilled water to prepare 1 M solution. For the sintering experiments, 3 g of powder were mixed with 0.28 mL of 1 M acetic acid solution and manually mixed in a mortar. After 5 min of manual mixing, the powder was poured into a 20 mm diameter WC die. To prevent direct contact between the die and the powder, a graphite foil was placed between the powder and each punch, and the inner wall of the die was covered with Kapton foil to prevent direct electrical contact between the die and the sample. A 100 MPa uniaxial pressure was applied and maintained constant throughout sintering process with an Atlas T25 automated hydraulic press during all experiments. Temperature and sintering time for the various samples prepared are described in the results section. After sintering, graphite foils were removed manually with a razor and sample surfaces were polished to remove graphite residues on surfaces before further characterizations could be performed.

In situ electrochemical impedance spectroscopy (EIS) measurements were achieved using a MTZ35 (Bilogic company) impedance analyzer in the frequency range 0.1 Hz - 1 MHz under an AC voltage of 100 mV. The measurements taken after sintering, when the sample was at room temperature, for a period of 200h. These were made with the sample still in the die, exposed to ambient air. The setup was Data were fitted with the Zview software (from Scribner Associates) using series R-CPE equivalent circuit.

Density of the samples were determined from their weight and geometrical measurements.

SEM observations were done with a TESCAN Vega 3 microscope using 10 kV acceleration voltage on fractured samples. XRD analyzes were achieved using a Bruker D4 Endeavor diffractometer with Cu-Kα radiation on 30-65° (2θ range), on both polished surfaces and powders obtained from crushed sintered pellets.

Diffuse reflectance spectra were recorded using a Cary 5000 UV-vis spectrometer for evaluation of the band gap of ZnO nanoparticles. Thermo Gravimetric Analyzes were performed with a Mettler Toledo TGA/DSC equipment with a 10 °C/min thermal ramp from room temperature to 600 °C under air.

3. Results

The temperature and pressure profile of the samples prepared in this study is described in **Figure 1**. The impedance measurements were performed for all samples after 2h of cooling at the end of the dwell time, when the sample temperatures were back to room temperature. The measurements were then recorded every hour for 200h. Two samples were measured in this way in air without removing them from the die, after sintering them at 200 and 250 °C respectively, based on the previous work [28]. The reason for such measurement setup relies on the necessity to avoid any remaining liquid phase evaporation from the die that would have occurred in case of metal paste application and heat treatment, or even with metal evaporation to deposit electrodes on the sample's surfaces.

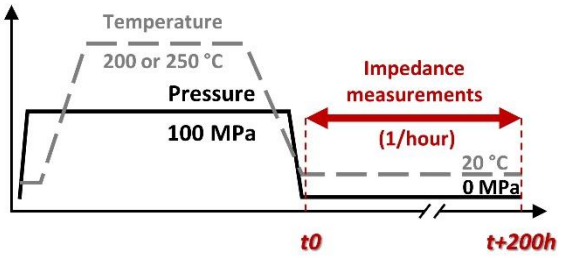

Figure 1: Temperature and pressure profile of experiments, showing the time periods for impedance measurements from t0 to t+200h after sintering dwell time finishes.

The EIS data of both samples sintered at 200 and 250 °C are presented in **Figure** 2. Firstly, the sample's data must be decomposed in two sets of data: i) a low frequency straight line (see **Figure** 2a inset) which can be attributed to the contribution arising from remaining acetates in the ZnO grain-grain interfaces, and ii) a higher frequency loop arising from ZnO electronic conductivity (as previously described in [28]). Comparing both samples (200 and 250 °C), it clearly appears that the acetate contribution is only visible after 200 °C sintering, while at 250 °C, only the ZnO contribution is observed (see **Figure 2b**). Another feature arising from these data relates to the time dependance of EIS data. After 200 °C

sintering, only a slight evolution of resistivity between 2 and 100h is observed, while no evolution is detected between 100 and 200h. This implies a quasi-stable electrical behavior of the sample after sintering. On the other hand, the sample sintered at 250 °C shows a noticeable evolution of impedance during the whole time from 2 up to 200h. This observation suggests a strong evolution of the material that may arise from microstructural evolution, chemical reactions, or interfaces modifications.

To have a closer look at the ZnO contribution for both samples, Figure2 c&d for the 200 °C and e&f for the 250 °C sample, a magnified view of imaginary part of impedance is plotted versus real part on one side (Nyquist plots) and versus frequency on the other side. These data were fitted using a R-CPE equivalent circuits to fit the ZnO contribution to impedance, regardless of the acetate part at low frequency for **Figure 2 c&d**. These plots highlight the presence actually two contributions in the loop, that must be used to fit the experimental data. These can be ascribed to grains (highest frequency) and grain boundaries (GB) at lower frequency.

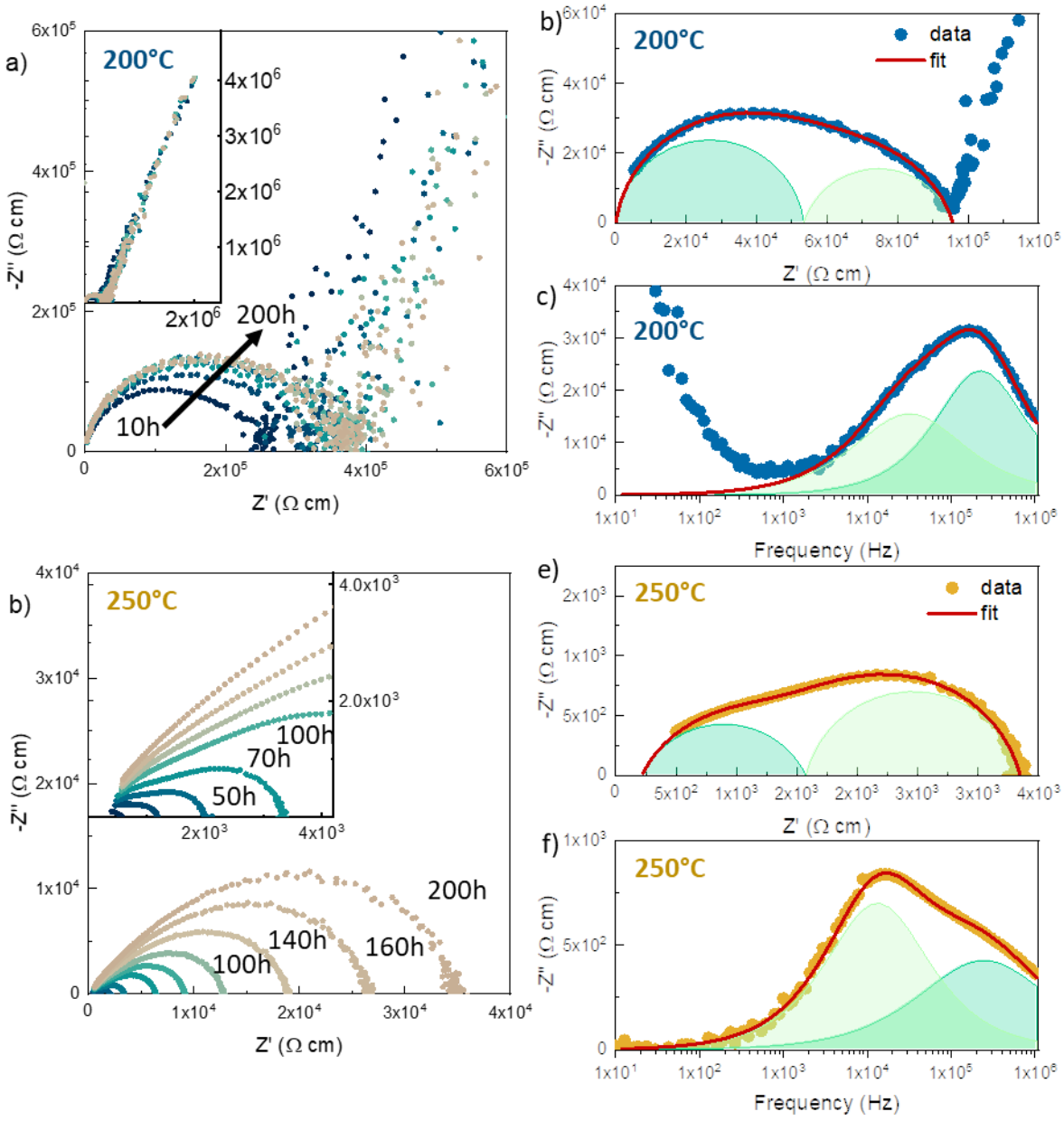

Figure 2: Impedance data recorded after sintering and after cooling down to room temperature, for 200h after sintering for the sample sintered at a-c) 200 °C and d-f) 250 °C; a) & d) correspond to Nyquist plots at different selected ageing times, while b-c) correspond to a magnified view of Nyquist and Bode plots respectively, for the sample sintered at 200 °C after 5h, while e-f) correspond to the one sintered at 250 °C after 40h. The fits rely on a equivalent circuit made of 2 R-CPE connected in series to model the ZnO impedance behaviour.

To investigate the impedance evolution, data fitting was done for both samples over the ageing time up to 200h after sintering. These fits were done on the ZnO contribution (> 100 Hz) considering 2 R-CPE contributions [29,30]. From the fitted data, three data are obtained: i) R: resistance (in Ω), ii) Q: CPE simulation parameter related to capacitance and iii) n: dimensionless parameter ranging from 0 to 1. R was extracted and used to calculate resistivity according to:

$$\rho = R.\frac{A}{t} \quad (1)$$

Where ρ is the resistivity (in Ω cm), A and t the area (in cm²) and thickness (in cm) of the sample measured geometrically. Then, Q and n were also used to calculate the equivalent capacitance C_{eq} using [29]:

$$C_{eq} = (R^{1-n}.Q)^{1/n} \quad (2)$$

The resulting data were plotted versus temperature both for the GB and grains contributions (see **Figure 3**). The sample sintered at 200 °C shows small evolution of both ρ and C_{eq}, while the sample sintered at 250 °C shows a huge evolution during the whole ageing time. Both grains and GB resistivities increase by few orders of magnitude. However, the main evolution is seen for the GB, with more than x500 higher ρ_{GB} after 200h (compared to x15 for ρ_{grain}). In the meantime, the value of C_{eq} is almost stable for the grains (C_{grain}(t+30h) / C_{grain}(t+200h) = 1.01), while it decreases strongly for the GB (C_{GB}(t+30h) / C_{GB} (t+200h) = 30).

According to these observations, two questions arise: i) why is there an evolution of impedance properties of the sample sintered at 250 °C while no clear evolution is visible after sintering at 200 °C, and ii) what is the mechanism involved that could explain why GB are more affected than grains in terms of electrical properties.

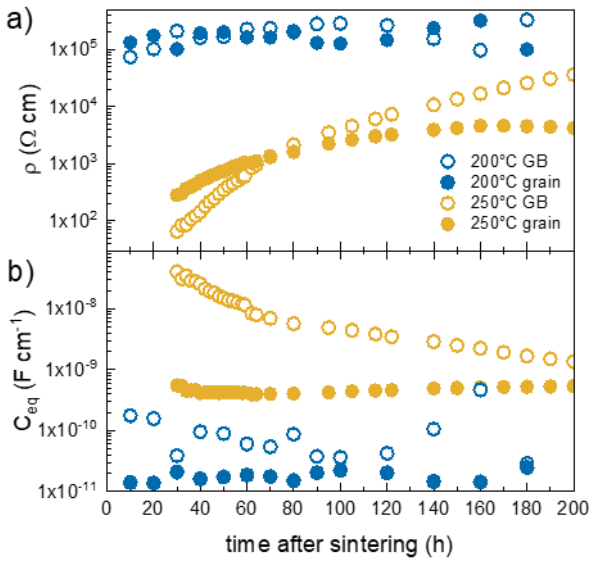

Figure 3: Fitting results from EIS data showing a) resistivity and b) equivalent capacitance for grains and GB contributions to impedance

To investigate these, two other samples were prepared with the same sintering conditions (temperature, pressure and time), and were immediately characterized and compared to the first two aged samples (sample named t0 and t+200h). **Figure** 4 displays the SEM observations made on fractured samples at 2 different magnification levels. As expected, the grain sizes are affected by the sintering temperature with a clear increase from 200 to 250 °C (~ 0.3 to 1.1 µm). However, on the basis of these observations, no drastic evolution from t0 to t+200h can be evidenced, whatever the sintering temperature. This excludes that the evolution of impedance after 250 °C sintering arises from a microstructural evolution (grain size increase or decrease, porosity formation). As expected, samples densities, summarized in table 1, confirm the absence of evolution after ageing at room temperature.

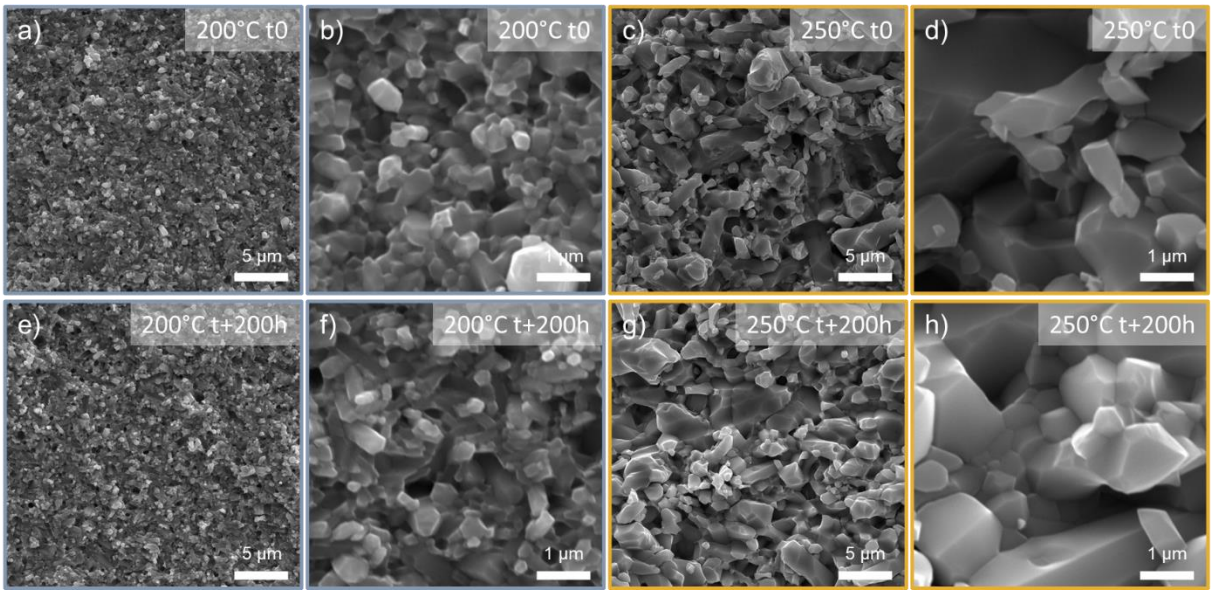

Figure 4: SEM images of fractured samples sintered without ageing at (a-b) 200 °C,(c-d) 250 °C and samples aged 200h before observation, sintered at (e-f) 200 °C and (g-h) 250 °C

Table 1: Densities measured on pellets after sintering at 200 and 250 °C and different ageing time at room temperature

	t0	**t+200h**
200 °C	97.5 ± 0.5%	97.9 ± 0.5%
250 °C	97.9 ± 0.5%	98.1 ± 0.5%

Diffuse reflectance measurements were performed and Tauc plots ($\alpha h\nu^2$ vs. $h\nu$, where α stands for the relative absorption and $h\nu$ the photon energy) were drawn to determine the optical band gap of these samples. All of them exhibit a similar behavior, showing a clear band gap of

~3.1 eV, which is typical of a ZnO ceramic [31,32]. However, while giving a closer look to the evolution of this band gap between samples freshly sintered and aged ones, one can notice a slight increase of 0.1 eV for both sintering temperatures.

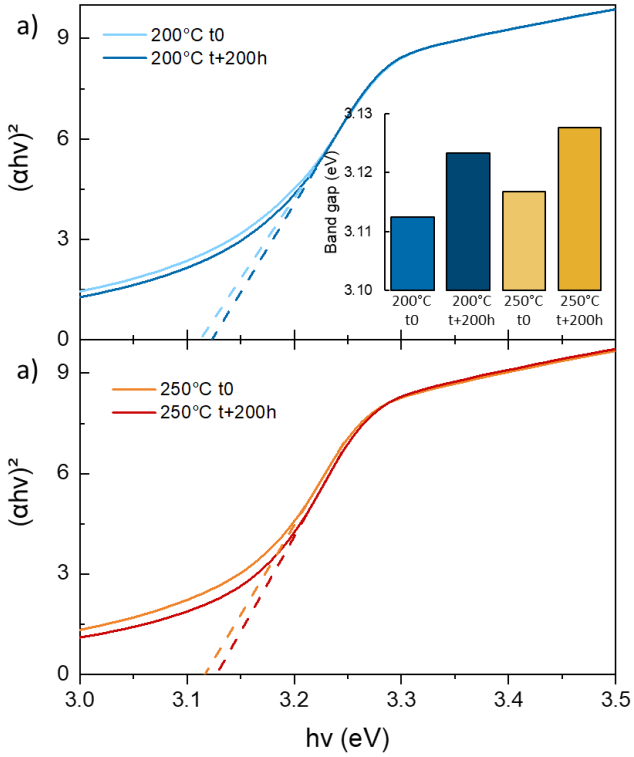

Figure 5: Tauc plots of diffuse reflectance of ZnO ceramics sintered at a) 200 °C and b) 250 °C without ageing and after 200h ageing at room temperature

Additionally, the samples were characterized by XRD. As shown on all patterns, all peaks belong to ZnO wurtzite phase, and no evidence of a second phase, due to transition nor decomposition of the material, can be detected. These patterns were then used to perform a profile refinement (see supplementary **Figure S1**), showing a good agreement with the *P6/3mc* space group, and good χ^2 reliability factors. These refinements were used to determine cell parameters and volumes that are reported in **Figure** 6b. They show that both samples at t0 show similar lattice parameters (see also **Figure S2** summarizing the a, c and cell volumes of the different samples), while they both exhibit a cell volume (along with a and c, although less pronounced for c parameter at 250 °C) reduction after 200h of ageing at room temperature. Although it is slightly higher for the sample sintered at 200 °C than 250 °C (-0.027 $Å^3$ and -0.016 $Å^3$ respectively) they tend to show a similar behavior.

For the two samples sintered at 200 °C and the 250 °C t0, no crystallite size can be determined since the only peak broadening observed is related to instrumental contribution (crystallite sizes

> 200 nm). Conversely, the 250 °C samples show a different behavior. While at t0, no clear difference can be visible with 200 °C samples, it shows a drastic evolution after 200h ageing, with a peak broadening, related to a crystallite size reduction to ~50 nm (obtained from XRD refinement).

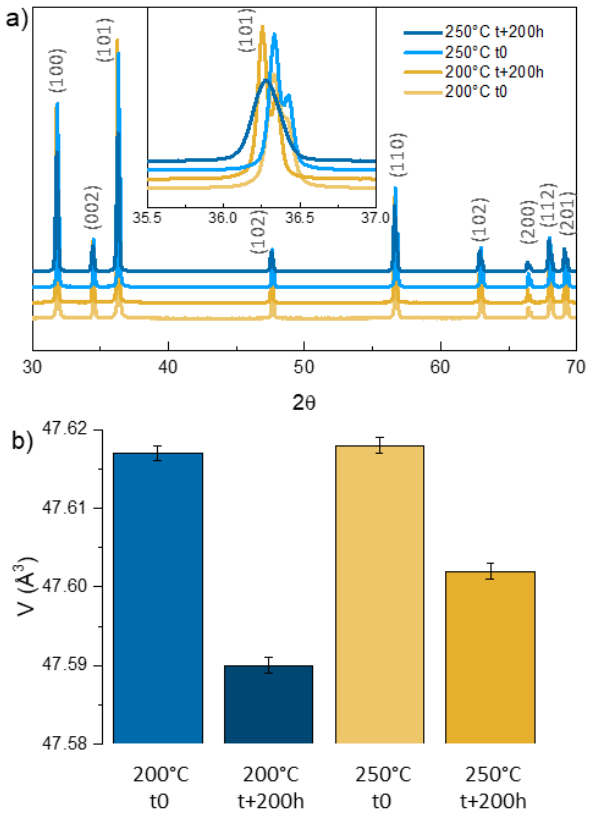

Figure 6: a) XRD patterns of samples sintered at 200 and 250 °C, aged 200h and not aged (figure inset corresponds to a magnification of the main (101) peak) and b) the refined lattice cell volumes of each sample.

4 – Discussion

The crystallite size reduction, determined from XRD analysis on the sample aged at 250°C, can be surprising by two aspects: i) no grain size reduction has been observed in the SEM images performed on the sample aged 200h and ii) there is no apparent reason for a room temperature evolution of the microstructure.

However, one explanation can be invoked, dealing with the presence of remaining acetates after sintering. In the present work, CSP was done in the presence of acetic acid for all samples, which is known to have a strong influence on the dissolution-precipitation of ZnO, not only during CSP [23,33,34], but also in mild conditions [35]. One could expect that the remaining acetates present in the porosities and/or grain boundaries (between adjacent grains) play a role in the evolution of these grain boundaries chemistry and properties.

To check whether acetates species remain present in the samples after sintering, TGA analyses were performed on 2 samples aged 200h after sintering at 200 and 250 °C. The results are presented in **Figure 7** and show two mass losses for the sample sintered at 250 °C. The weight loss < 100 °C can be assigned to physiosorbed water, while the one at 330 °C (also visible on the sample sintered at 200 °C) has been previously attributed to the decomposition of acetates [23]. This confirms the presence of remaining acetates in both samples, even for the 250 °C one, where the EIS seems to indicate the absence of acetate contribution. In the meantime, the sample at 200 °C shows both the presence of acetates in TGA and EIS.

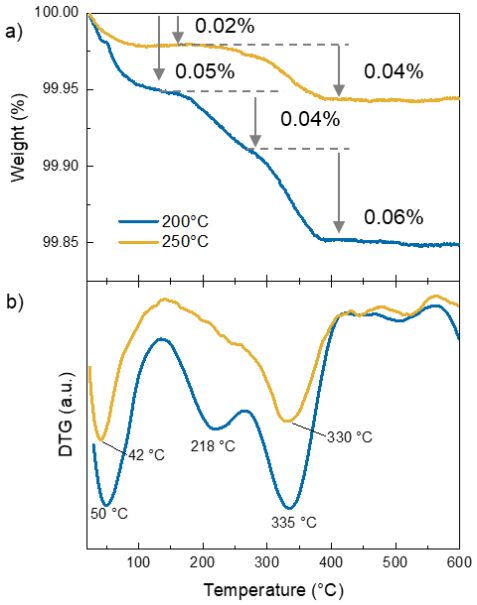

Figure 7: a) TGA and b) DTG analysis of samples sintered at 200 and 250 °C and aged 200h before measurement

To explain why acetate presence can be confirmed by TGA while not being detected by EIS, one has to consider the fact that in the electrical pathway for EIS measurement, the current has to flow through the major phase (ZnO). However, it does not have to flow through the acetate layers (in GB) if there is a possible path through purely ZnO. This comes from the fact that acetates will increase the overall resistance (grains + GB + acetates). Thus, acetates are eliminated from GBs but are still present in triple points, it could not be detected by EIS.

In the case of the sample sintered at 200 °C, the acetates must be present in all GBs as Zn acetates stable species [25,33]. Thus, the measured EIS is stable after sintering as no chemical

reaction occurs at room temperature and pressure after sintering, although the electrical conductivity is lowered by the presence of these acetates.

In the case of the sample sintered at 250 °C, acetates started to be eliminated, and GBs free from acetate started to form, increasing the GB conductivity [28]. However, some acetate must be trapped into triple junctions, and could not be evacuated at the end of sintering. This has led to the situation drawn in **Figure 8**. After coming back to room temperature and pressure, EIS shows a strong evolution of resistivity and capacitance, especially for GBs. This suggests that the trapped acetates may have interacted through further dissolution-precipitation reactions probably occurring by reaction/diffusion along the GBs, as presented in **Figure 8**. This dissolution-reprecipitation may leading to nucleation of small particles (as observed in CSP of Bi_2O_3 by Tsuji *et al.* [36]), leading to wider XRD peaks, smaller crystallite size and generating defects in the lattice. This phenomenon is similar to what has been shown by Taveri *et al.* in the case of densification of silica after room temperature ageing [37]. According to the evolution of EIS data, these interactions keep on working during more than 200h after cooling back to room temperature.

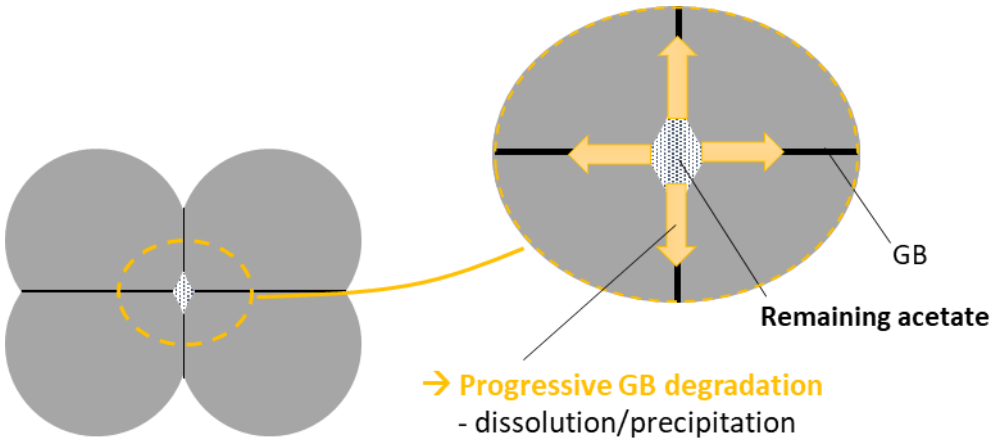

Figure 8: Schematic representation of the GB degradation process after sintering at 250 °C in the presence of remaining acetates inside the porosities.

According to the lattice size reduction, along with band gap increase and grain impedance evolution, there must be reaction of ZnO with acetates also located in the bulk. However, its magnitude must be much lower than the one encountered in GB. Since most of the acetate/ceramic interactions at room temperature should occur in GB, and because grain sizes (according to SEM observations) are > 500 nm, GB represent a very small amount of matter,

in comparison with grains. Therefore, only characterization techniques that are sensitive to these GB, such as impedance measurements, can highlight their evolution.

Therefore, two main phenomena must occur in the present case: i) a GB localized degradation due to the presence of remaining acetates after sintering, leading to huge impedance modification after sintering at 250 °C, where part of GB were clean from acetates; and ii) a bulk interaction with acetates, leading to slight evolution of lattice volumes, band gaps, and grain conductivity. This latter leads a quite important bulk evolution at 250 °C, where conductivity is almost 3 orders of magnitude higher than after 200 °C sintering (at t0). Conversely, it is of much lower magnitude in the sample sintered at 200 °C, since the acetate species remain present after sintering in the whole interface regions.

To better describe the evolution of the remaining liquid phase in porosities, one possibility would be to analyze the sintered samples during ageing with SAXS methods, as recently developed for *in situ* measurements during Cold Sintering by Allen *et al.* [38,39]. It may allow to track the possible elimination of liquid though solid/liquid reaction and the formation of gas phase, probably trapped in the remaining porosity.

5. Conclusions

This work highlights the room temperature evolution of ZnO ceramics prepared by CSP with acetic acid. The characterizations before and after ageing, but also *in situ* during this ageing at room temperature for 200h show that:

i. ZnO bulk and GB resistivity remain stable after 200 °C sintering, while they both gain few orders of magnitude after sintering at 250 °C and ageing at room temperature;
ii. Most of the evolution deals with the GB contribution, pointing its implication in possible chemical reactions at interfaces;
iii. Acetate species, although not contributing to impedance, are not eliminated and remain present after sintering at 250 °C, leading to a room temperature evolution of the sample's properties;
iv. ZnO grains face only slight changes of crystallinity and optical properties, pointing the more important evolution located at GB

This work shows the importance of paying attention to the possible evolution of ceramics after CSP treatment, particularly if the elimination of liquid phase is not complete. It also shows that a very small amount of this liquid phase may have an important impact on the resulting

properties of the samples sintered. Moreover, it highlights the predominance of GB reactivity, requiring characterization techniques dedicated to their analyses. This way, impedance analysis has shown great sensitivity and capability to detect slight evolutions in these GB, and present a great tool to characterize cold sintered materials.

6. References

[1] N. Yamasaki, K. Yanagisawa, M. Nishioka, S. Kanahara, A hydrothermal hot-pressing method: apparatus and application, J Mater Sci Lett 5 (1986) 355–356.

[2] N. Yamasaki, T. Weiping, K. Jiajun, Low-temperature sintering of calcium carbonate by a hydrothermal hot-pressing technique, J Mater Sci Lett 11 (1992) 934–936.

[3] K. Yanagisawa, M. Nishioka, K. Ioku, N. Yamasaki, Densification of silica gels by hydrothermal hot-pressing, J Mater Sci Lett 12 (1993) 1073–1075.

[4] A. Ndayishimiye, A. Largeteau, S. Mornet, M. Duttine, M.-A. Dourges, D. Denux, M. Verdier, M. Goune, T. Herisson de Beauvoir, C. Elissalde, G. Goglio, Hydrothermal Sintering for Densification of Silica . Evidence for the Role of Water, J Eur Ceram Soc 38 (2018) 1860–1870. https://doi.org/10.016/j.jeurceramsoc.2017.10.011.

[5] A. Ndayishimiye, A. Largeteau, M. Prakasam, S. Pechev, M.A. Dourges, G. Goglio, Low temperature hydrothermal sintering process for the quasi-complete densification of nanometric α-quartz, Scr Mater 145 (2018) 118–121. https://doi.org/10.1016/j.scriptamat.2017.10.023.

[6] C. Drouet, C. Largeot, G. Raimbeaux, C. Estournès, G. Dechambre, C. Combes, C. Rey, Bioceramics: Spark Plasma Sintering (SPS) of Calcium Phosphates, Advances in Science and Technology 49 (2006) 45–50. https://doi.org/10.4028/www.scientific.net/ast.49.45.

[7] F. Brouillet, D. Laurencin, D. Grossin, C. Drouet, C. Estournes, G. Chevallier, C. Rey, Biomimetic apatite-based composite materials obtained by spark plasma sintering (SPS): physicochemical and mechanical characterizations, J Mater Sci Mater Med 26 (2015) 1–11.

[8] H. Guo, A. Baker, J. Guo, C.A. Randall, Cold Sintering Process: A Novel Technique for Low-Temperature Ceramic Processing of Ferroelectrics, Journal of the American Ceramic Society 99 (2016) 3489–3507.

[9] J. Guo, H. Guo, A.L. Baker, M.T. Lanagan, E.R. Kupp, G.L. Messing, C.A. Randall, Cold Sintering : A Paradigm Shift for Processing and Integration of Ceramics, Angewandte Chemie Communications 55 (2016) 11457–11461.

[10] H. Guo, A. Baker, J. Guo, C.A. Randall, Protocol for Ultralow-Temperature Ceramic Sintering: An Integration of Nanotechnology and the Cold Sintering Process, ACS Nano 10(11) (2016) 10606–10614.

[11] J. Guo, H. Guo, D.S.B. Heidary, S. Funahashi, C.A. Randall, Semiconducting properties of cold sintered V2O5 ceramics and Co-sintered V2O5-PEDOT:PSS composites, J Eur Ceram Soc 37 (2016) 1529–1534. https://doi.org/10.1016/j.jeurceramsoc.2016.11.021.

[12] X. Zhao, J. Guo, K. Wang, T. Herisson De Beauvoir, B. Li, C.A. Randall, Introducing a ZnO-PTFE (Polymer) Nanocomposite Varistor via the Cold Sintering Process, Adv Eng Mater 20 (2018) 1700902. https://doi.org/10.1002/adem.201700902.

[13] T. Hérisson de Beauvoir, K. Tsuji, X. Zhao, J. Guo, C. Randall, Cold sintering of ZnO-PTFE: Utilizing polymer phase to promote ceramic anisotropic grain growth, Acta Mater 186 (2020). https://doi.org/10.1016/j.actamat.2020.01.002.

[14] T. Herisson de Beauvoir, S. Dursun, L. Gao, C. Randall, New Opportunities in Metallization Integration in Cofired Electroceramic Multilayers by the Cold Sintering Process, ACS Appl Electron Mater 1 (2019) 1198–1207. https://doi.org/10.1021/acsaelm.9b00184.

[15] S. Funahashi, H. Guo, J. Guo, A.L. Baker, K. Wang, K. Shiratsuyu, C.A. Randall, Cold sintering and co-firing of a multilayer device with thermoelectric materials, Journal of the American Ceramic Society 100 (2017) 3488–3496. https://doi.org/10.1111/jace.14852.

[16] T. Sada, K. Tsuji, A. Ndayishimiye, Z. Fan, Y. Fujioka, C.A. Randall, High permittivity BaTiO3 and BaTiO3-polymer nanocomposites enabled by cold sintering with a new transient chemistry: Ba(OH)2·8H2O, J Eur Ceram Soc (2020). https://doi.org/10.1016/j.jeurceramsoc.2020.07.070.

[17] K. Tsuji, A. Ndayishimiye, S. Lowum, R. Floyd, K. Wang, M. Wetherington, J. Maria, C.A. Randall, Single Step Densification of High Permittivity BaTiO3 Ceramics at 300 oC, J Eur Ceram Soc 40 (2020) 1280–1284. https://doi.org/10.1016/j.jeurceramsoc.2019.12.022.

[18] T. Herisson De Beauvoir, C. Estournès, Translucent γ-AlOOH and γ-Al2O3 glass-ceramics using the cold sintering process, Scr Mater 194 (2021) 113650. https://doi.org/10.1016/j.scriptamat.2020.113650.

[19] J. Guo, R. Floyd, S. Lowum, J.-P. Maria, T. Herisson De Beauvoir, J.H. Seo, C.A. Randall, Cold Sintering: Progress, Challenges, and Future Opportunities, Annu Rev Mater Res 49 (2019) 275–95. https://doi.org/10.1146/annurev-matsci-070218- 010041.
[20] S. Grasso, M. Biesuz, L. Zoli, G. Taveri, A.I. Duff, D. Ke, A. Jiang, M.J. Reece, A review of cold sintering processes, Advances in Applied Ceramics 119 (2020) 115–143. https://doi.org/10.1080/17436753.2019.1706825.
[21] A. Ndayishimiye, M.Y. Sengul, D. Akbarian, Z. Fan, K. Tsuji, S.H. Bang, A.C.T. Van Duin, C.A. Randall, Dynamics of the Chemically Driven Densification of Barium Titanate Using Molten Hydroxides, Nano Lett 21 (2021) 3451–3457. https://doi.org/10.1021/acs.nanolett.1c00069.
[22] A. Ndayishimiye, S.H. Bang, Christopher.J. Spiers, C.A. Randall, Reassessing cold sintering in the framework of pressure solution theory, J Eur Ceram Soc (2022). https://doi.org/10.1016/j.jeurceramsoc.2022.09.053.
[23] S. Funahashi, J. Guo, H. Guo, K. Wang, A.L. Baker, K. Shiratsuyu, C.A. Randall, Demonstration of the Cold Sintering Process Study for the Densification and Grain Growth of ZnO Ceramics, Journal of the American Ceramic Society 100 (2017) 546–553. https://doi.org/10.1111/jace.14617.
[24] J. Gonzalez-Julian, K. Neuhaus, M. Bernemann, J. Pereira da Silva, A. Laptev, M. Bram, O. Guillon, Unveiling the mechanisms of cold sintering of ZnO at 250 °C by varying applied stress and characterizing grain boundaries by Kelvin Probe Force Microscopy, Acta Mater 144 (2018) 116–128. https://doi.org/10.1016/j.actamat.2017.10.055.
[25] A. Jabr, J. Fanghanel, Z. Fan, R. Bermejo, C. Randall, The effect of liquid phase chemistry on the densification and strength of cold sintered ZnO, J Eur Ceram Soc 43 (2023) 1531–1541. https://doi.org/10.1016/j.jeurceramsoc.2022.11.071.
[26] Y. Jing, N. Luo, S. Wu, K. Han, X. Wang, L. Miao, Y. Wei, Remarkably improved electrical conductivity of ZnO ceramics by cold sintering and post-heat-treatment, Ceram Int 44 (2018) 20570–20574.
[27] J. Chevalier, L. Gremillard, S. Deville, Low-temperature degradation of zirconia and implications for biomedical implants, Annu Rev Mater Res 37 (2007) 1–32. https://doi.org/10.1146/annurev.matsci.37.052506.084250.
[28] T. Hérisson de Beauvoir, P.L. Taberna, P. Simon, C. Estournès, Cold Sintering Process characterization by in operando electrochemical impedance spectroscopy, J Eur Ceram Soc 42 (2022) 5747–5755. https://doi.org/10.1016/j.jeurceramsoc.2022.05.077.
[29] J. Fleig, The grain boundary impedance of random microstructures: numerical simulations and implications for the analysis of experimental data, Solid State Ion 150 (2002) 181–193. www.elsevier.com/locate/ssi.
[30] C. Kjølseth, H. Fjeld, Ø. Prytz, P.I. Dahl, C. Estournès, R. Haugsrud, T. Norby, Space-charge theory applied to the grain boundary impedance of proton conducting BaZr0.9Y0.1O3 - δ, Solid State Ion 181 (2010) 268–275. https://doi.org/10.1016/j.ssi.2010.01.014.
[31] L. Kumar Jangir, Y. Kumari, A. Kumar, M. Kumar, K. Awasthi, Investigation of luminescence and structural properties of ZnO nanoparticles, synthesized with different precursors, Mater Chem Front 1 (2017) 1413–1421. https://doi.org/10.1039/c7qm00058h.
[32] J. Wang, Z. Wang, B. Huang, Y. Ma, Y. Liu, X. Qin, X. Zhang, Y. Dai, Oxygen vacancy induced band-gap narrowing and enhanced visible light photocatalytic activity of ZnO, ACS Appl Mater Interfaces 4 (2012) 4024–4030. https://doi.org/10.1021/am300835p.
[33] M.Y. Sengul, C.A. Randall, A.C.T. Van Duin, ReaxFF Molecular Dynamics Study on the Influence of Temperature on Adsorption, Desorption, and Decomposition at the Acetic Acid/Water/ZnO(1010) Interface Enabling Cold Sintering, ACS Appl Mater Interfaces 10 (2018) 37717–37724. https://doi.org/10.1021/acsami.8b13630.
[34] A. Ndayishimiye, M.Y. Sengul, S.H. Bang, K. Tsuji, K. Takashima, T. Hérisson de Beauvoir, D. Denux, J.M. Thibaud, A.C.T. van Duin, C. Elissalde, G. Goglio, C.A. Randall, Comparing hydrothermal sintering and cold sintering process: Mechanisms, microstructure, kinetics and chemistry, J Eur Ceram Soc 40 (2020) 1312–1324. https://doi.org/10.1016/j.jeurceramsoc.2019.11.049.
[35] B. Dargatz, J. Gonzalez-Julian, O. Guillon, Anomalous coarsening of nanocrystalline zinc oxide particles in humid air, J Cryst Growth 419 (2015) 69–78. https://doi.org/10.1016/j.jcrysgro.2015.02.101.
[36] K. Tsuji, T. Herisson De Beauvoir, A. Ndayishimiye, K. Wang, C.A. Randall, Cold sintering of yttria-stabilized cubic bismuth oxide: Conductivity and microstructural evolution of metastable grain boundaries with annealing, J Appl Phys 128 (2020). https://doi.org/10.1063/5.0014287.
[37] G. Taveri, S. Grasso, F. Gucci, J. Toušek, I. Dlouhy, Bio-Inspired Hydro-Pressure Consolidation of Silica, Adv Funct Mater 28 (2018) 1805794. https://doi.org/10.1002/adfm.201805794.
[38] A.J. Allen, I. Levin, R.A. Maier, S.E. Witt, F. Zhang, I. Kuzmenko, In situ characterization of ceramic cold sintering by small-angle scattering, Journal of the American Ceramic Society 104 (2021) 2442–2448. https://doi.org/10.1111/jace.17664.

[39] F. Zhang, R.A. Maier, I. Levin, A.J. Allen, J.S. Park, P. Kenesei, I. Kuzmenko, P. Jemian, J. Ilavsky, In situ probing of interfacial roughness and transient phases during ceramic cold sintering process, Acta Mater 259 (2023). https://doi.org/10.1016/j.actamat.2023.119283.